The Quiescent Double Barrier Regime in the DIII–D Tokamak

E.J. Doyle,[1] L.R. Baylor,[2] K.H. Burrell,[3] T.A. Casper,[4] J.C. DeBoo,[2] D.R. Ernst,[5] A.M. Garofalo,[6] P. Gohil,[3] C.M. Greenfield,[3] R.J. Groebner,[3] A.W. Hyatt, [3] G.L. Jackson,[3] T.C. Jernigan,[2] J.E. Kinsey,[7] L.L. Lao,[3] C.J. Lasnier,[4] J.N. Leboeuf,[8] M. Makowski,[4] G.R. McKee,[9] R.A. Moyer,[10] M. Murakami,[2] T.H. Osborne,[3] W.A Peebles,[1] M. Porkolab,[11] G.D. Porter,[4] T.L. Rhodes,[1] J.C. Rost,[11] D. Rudakov,[10] G.M. Staebler,[3] B.W. Stallard,[4] E.J. Strait,[3] R. Sydora,[12] E.J. Synakowski,[5] G. Wang[1], J.G. Watkins,[13] W.P. West,[3] and L. Zeng[1]

[1]Dept. of Electrical Engineering and IPFR, University of California, Los Angeles, California 90095, USA

[2]Oak Ridge National Laboratory, Oak Ridge, Tennessee 37381, USA

[3]General Atomics, P.O. Box 85608, San Diego, California 92186, USA

[4]Lawrence Livermore National Laboratory, Livermore, California, 94550, USA

[5]Princeton Plasma Physics Laboratory, Princeton, New Jersey 08543, USA

[6]Columbia University , New York, New York 10027, USA

[7]Lehigh University, Bethlehem, Pennsylvania 18015, USA

[8]Physics Dept., University of California, Los Angeles, California 90095, USA

[9]University of Wisconsin-Madison, Madison, Wisconsin 53706, USA

[10]University of California, San Diego, California 92697, USA

[11]Massachusetts Institute of Technology, Cambridge, Massachusetts 02139, USA

[12]University of Alberta, Edmonton, Alberta, Canada

[13] Sandia National Laboratories, Albuquerque, New Mexico 87185, USA

ABSTRACT

Experiments on the DIII–D tokamak have identified a new sustained high-performance operating mode, termed the Quiescent Double Barrier (QDB) regime. The QDB regime combines internal transport barriers (ITBs) with a quiescent, ELM-free

H–mode edge, termed QH–mode, giving rise to separate core and edge transport barriers. These double barriers have been maintained for >3.5 s (~25 τ_E), demonstrating a long-pulse, quasi-steady-state capability. The combination of core ITBs and edge H–mode temperature pedestals results in high performance plasmas; a $\beta_N H_{89}$ product of 7 has been maintained for $10\tau_E$, other peak (non-simultaneous) parameters include $T_i \leq 17$ keV, $\beta_N \leq 2.9$ %-m-T/MA, $H_{89} \leq 2.6$, $\beta \leq 3.8\%$, $\tau_E \leq 160$ ms and DD neutron rate $S_n \leq 5.5 \times 10^{15}$ s^{-1}. These results address a major issue with tokamak plasmas; how to sustain long pulse, high performance H–mode plasmas without ELMs, yet retaining the density and impurity control hitherto provided by ELMs. In these QDB plasmas ELMs are replaced by continuous benign MHD activity in the edge, which enhances particle transport. A signature of operation with a QH–mode edge appears to be very large radial electric fields in the edge and SOL. In the core, simulations and modeling replicate many of the features of the observed transport and fluctuation behavior, including the ion temperature profile and turbulence correlation lengths. Slow high-Z impurity accumulation ($\tau \geq 500$ ms) is observed in the center of many QDB plasmas, and is the subject of ongoing analysis. To date the QDB regime has only been obtained in plasmas with counter-NBI (injection anti-parallel to the plasma current), and with divertor cryopumping to control the density.

1. INTRODUCTION

Next-step devices are anticipated to operate in the high confinement mode (H–mode), with edge localized modes (ELMs) for density, radiated power and impurity control [1]. However, ELMing H–mode plasmas have some non-optimal features, including: (1) Pulsed divertor heat and particle loads can lead to rapid erosion of the divertor plates [2], (2) Type I (giant) ELMs can inhibit or destroy the internal transport barriers (ITBs) desired for Advanced Tokamak (AT) operation and, (3) ELMs can couple to core MHD modes, and hence reduce the beta limit [3]. Internal transport barriers (ITBs, regions of reduced transport relative to L–mode), are also desirable in next-step devices; ITBs at large radii can improve fusion performance and stability

limits and result in favorable bootstrap alignment with the total current profile [4]. The results reported here demonstrate that sustained, high performance ELM-free H–mode plasmas are possible with good density and radiated power control. The results also demonstrate that the quiescent, ELM-free edge can easily be combined with core ITBs to obtain the benefits of both core and edge transport barriers.

The new Quiescent Double-Barrier (QDB) regime on DIII–D combines core transport barriers with a quiescent, ELM-free H–mode edge, termed QH–mode, giving rise to separate (double) core and edge transport barriers [4–6]. The combination of core ITBs and edge H–mode temperature pedestals results in improved performance relative to ITBs with an L–mode edge, or conventional ELMing H–mode. A $\beta_N H_{89}$ product of 7 has been achieved for 10 τ_E with QDB operation, substantially superior to "standard" H–mode levels of $\leq$ 4–5. ($\beta_N H_{89}$ is a figure of merit for AT machines, where $\beta_N = \beta/(I/aB_\phi)$ and $H_{89} = \tau_E/\tau_{89}$, where τ_{89} is a global confinement scaling expression for L–mode plasmas [7]). QDB operation has been sustained for >3.5 s (~25 τ_E), demonstrating a long-pulse, quasi-steady-state capability. Simulations and modeling replicate many of the features of the observed core transport and fluctuation behavior, including the ion temperature profile and turbulence correlation lengths.

The work reported here stems from efforts on DIII–D to control and optimize internal transport barriers [4,8]. The combined H–mode edge and core transport barriers in QDB plasmas result in broadened profiles and improved stability compared with an ITB alone. Previous attempts on DIII–D to combine ITBs with ELMing H–mode edges did not yield high quality ITBs [9]. Specifically, ELM penetration to the core limited ITB development [9], while operation with a conventional ELM-free edge led to a steadily increasing and destabilizing edge pressure gradient [10]. Double barriers in the form of ITBs plus an ELMing H–mode edge have been obtained previously on larger devices such as JT-60U [11,12] and JET [13], where the greater physical separation between the edge pedestal and the ITBs helps, and on ASDEX-U by careful tailoring of the ELM characteristics [14]. A feature of the QDB regime on DIII–D is that the edge

and core transport barriers are compatible and do not merge or negatively impact one another.

The remainder of this paper is structured as follows. An overview of QDB operation is presented in Section 2, while the following sections consider in more detail the physics of the QH-mode edge (Section 3), and issues associated with core aspects of QDB operation, such as transport and fluctuation behavior (Section 4). A summary is presented in Section 5. Several new acronyms are introduced in this paper, which are summarized here: QDB — quiescent double barrier, QH–mode — quiescent H–mode, and EHO — edge harmonic oscillation.

2. OVERVIEW OF QUIESCENT DOUBLE BARRIER OPERATION

In this section we present an overview of operation in the Quiescent Double Barrier (QDB) regime. An example of the time evolution of a QDB plasma is shown in Fig. 1. This discharge has $I_p = -1.3$ MA (i.e. reversed current, so as to obtain counter-NBI) and $B_T = 2.0$ T. The plasma makes a transition to H–mode shortly after counter-NBI heating is applied at 0.8 s. After an initial ELMing phase the discharge evolves into a quiescent phase (QH–mode), as marked by the disappearance of bursts on the D_α emission. During this quiescent phase the line average density and radiated power become essentially constant, indicating that edge particle transport is sufficiently large for divertor cryopumping to control the density and low-Z impurity content. Also during the QH–mode phase, a continuous oscillation is shown on magnetic probe signals after the ELMs cease, Fig. 1(f). This is the edge harmonic oscillation (EHO), which will be discussed later in Section. 3.3. This discharge remains ELM-free with a quiescent H–mode edge for over 3.5 s, or about 25 τ_E, limited only by the duration of the NBI heating sources.

An ITB forms during the QH–mode period of the discharge shown in Fig. 1, resulting in improved core performance and creating a QDB plasma. $\beta_N H_{89}$ rises continuously throughout the discharge to ~6%-m-T/MA, Fig. 1(e). The edge and core barriers obtained with QDB operation are clearly seen in the temperature profiles shown

in Fig. 2. For comparison, profiles are also shown from a counter-NBI ITB discharge with an L–mode edge and a standard L–mode plasma. The QH–mode edge results in broader profiles with improved MHD stability compared with an ITB alone. The improved stability properties are demonstrated by the long pulse capability of the QDB regime, and global stability to low order n=1–2 ideal ballooning modes has been confirmed by modeling. That QDB plasmas can have significant central density peaking is shown in Fig. 2(d). The *q* profile, Fig. 2(c), is moderately reversed (NCS operation), and the foot of the core transport barrier lies substantially outside $\rho_{q_{min}}$.

The QH–mode edge is obtained with counter-NBI at power levels down to ~2.5 MW (at low current), and with divertor pumping to reduce and control the density. Addition of a core ITB inside the QH–mode edge to form a QDB plasma is straightforward using standard ITB formation techniques [8,15] and higher heating powers ($P_{NBI} \geq 7$ MW, though there is no sharp threshold). The QH–mode edge is characterized by continuous benign MHD activity, which usually takes the form of an edge harmonic oscillation (EHO), visible on magnetic, density and temperature fluctuation measurements. As discussed in Section 3.3, particle transport associated with the EHO appears to be responsible for the ability to maintain density and radiated power control in the ELM-free QH–mode regime. Another signature of QH–mode operation discussed in the same subsection is that there appear to be very large radial electric fields in the edge and SOL during QH–mode.

With regard to the core ITBs, the observed transport and fluctuation behavior is in reasonable agreement with modeling and simulations. As discussed in Section 4.2, the core ion temperature profile has been replicated based on the regulation of turbulent transport by ExB shear, while initial gyrokinetic modeling of ITG turbulence replicates the measured core turbulence correlation lengths. However, the observation of neoclassical ion transport with finite turbulence levels requires further measurements and modeling. In addition, measurements indicate that the core and edge transport barriers in QDB plasmas are separated by a region of low E×B flow shear. An issue still

under study is slow ($\tau \geq 500$ ms) high-Z impurity accumulation in the plasma center, which is often observed in these QDB plasmas.

3. THE QUIESCENT H–MODE EDGE

The key element in obtaining a QDB discharge is to create a quiescent, ELM-free H–mode edge (QH–mode). In this section we discuss the experimental requirements for obtaining QH–mode, edge and divertor conditions during QH–mode operation, MHD oscillations associated with QH–mode operation, and possible ELM stabilization mechanisms.

3.1. Operational conditions required to obtain QH–mode

The operational conditions required to access QH–mode can be summarized as follows:

1. Counter-NBI (injection anti-parallel to the plasma current), at power levels down to ~2.5 MW (at low current). As discussed further in Section 3.2 below, counter-NBI has different edge ion orbits as compared with co-NBI.
2. Divertor cryopumping to control the density, coupled with low line average densities of ~2–3×10^{19} m^{-3}. Typically, the only external particle fueling to QH–mode discharges during current flattop is that provided by the NBI.
3. A larger than usual gap between the plasma edge and the outer wall (low field side) of ~ 10 cm. Again this is probably related to the different edge ion orbits associated with counter-NBI, and a larger outer gap is required to prevent ions from interacting with the wall.

To date, QH–mode has been obtained in both upper and lower single-null discharges and across the following parameter range: $0.67 \leq I_p$ (MA) ≤ 1.6, $0.95 \leq B_T$ (T) ≤ 2.1, triangularity δ (of the side opposite the active X–point), of 0.16–0.7 and q of 3.7–4.6. Most work has been performed at $1.2 \leq I_p$ (MA) ≤ 1.6, $1.8 \leq B_T$ (T) ≤ 2.1, and $\delta \sim 0.4$. In addition, QH–mode has been obtained with both orientations of ∇B with respect to the divertor X–point.

3.2. Edge and divertor conditions during QH–mode operation

Edge pedestal conditions during both the quiescent and ELMing phases of a single discharge are shown in Fig. 3. As can be seen, the edge gradients are similar or higher in the quiescent as compared with the ELMing phase, demonstrating that the quiescent phase is indeed a true H–mode regime. QH–mode also has other standard H–mode signatures, including an edge E_r well with high E×B shear, an associated zone of reduced turbulence, and improved confinement. Also notable in Fig. 3 are the low pedestal density and high pedestal temperatures, particularly for ions, which can reach ~7 keV.

Shown in Fig. 4 is a comparison of edge pedestal conditions in QH–mode with those in the Type I and Type III ELMing regimes. From Fig. 4(a) it can be seen that the QH–mode occurs at low normalized pedestal densities and high temperatures. The points from the ELMing phases of QH–mode discharges support the conclusion from Fig. 3 that the edge electron pedestal conditions are unchanged from the ELMing to quiescent phases of these discharges. Whether the ELMs in the pre QH–mode phase are low density Type III ELMs is still under study. That the edge pressure gradient in QH–mode is at or above the ideal ballooning mode limit is shown in Fig. 4(b), though the edge gradient is less than for Type I ELMs. As the pressure limit was calculated using twice the electron pressure gradient, the data shown here may underestimate the edge pressure because of the substantial edge ion temperatures previously referred to. These data also show that the QH–mode edge pressure gradient increases with triangularity, as in standard ELMing H–mode [16]. These observations are consistent with an extensive body of prior work on ELM stability on DIII–D, which suggests that the edge stability limit may be set by kink/ballooning modes, and considerations of second stability access [16].

The low QH–mode edge densities and high temperatures result in a sheath limited, collisionless edge, raising concerns about divertor heat flux loading. Surprisingly, the conducted heat flux remains relatively modest. Shown in Fig. 5 is a comparison of the

heat flux to the outer divertor strike point, as determined from IR camera data, for a conventional high density H–mode plasma ($\bar{n}_e$ = 8×10^{19} m^{-3}, $P_{NB\ I}$= 4.5 MW), a low density H–mode plasma ($\bar{n}_e$ = 3.6×10^{19} m^{-3}, P_{NBI} = 6.25 MW), and a QDB plasma ($\bar{n}_e$ = 2×10^{19} m^{-3}, P_{NBI} = 7 MW). As can be seen, the divertor heat flux is actually lower for the QDB plasma as compared with the low density H–mode case and, allowing for the difference in input power, only ~30% higher than the high density conventional H–mode case. This reasonable divertor heat flux during QDB operation may be due to spreading of the heat load by the edge harmonic oscillation (EHO), discussed in the next subsection, but this requires further study. In addition, and in contrast to conventional ELMing H–mode, pulsed heat loads to the divertor are completely absent with QH–mode operation. On a more general level it should be noted that present-day devices can match anticipated core or edge reactor conditions, but not both simultaneously [1]. It follows, therefore, that present-day devices with reactor relevant cores, such as the QDB plasmas presented here, may have non-optimal divertor conditions.

There is one significant difference in edge conditions observed between QH–mode operation and conventional ELM-free or ELMing H–mode. As can be seen from CER derived measurements of the edge radial electric field, E_r, shown in Fig. 6(a), QH–mode has a several times deeper E_r well inside the separatrix than a conventional co-NBI discharge at comparable power. In addition, E_r on the open field lines in the scrape-off layer (SOL) outside the separatrix is also much higher. That the SOL plasma during QH–mode operation has E_r values usually associated with the H–mode edge transport barrier has been confirmed by data from a reciprocating Langmuir probe at the vessel midplane, Fig. 6(b). That these high E_r values in the SOL are directly associated with QH–mode operation, and not with H–mode operation with counter-NBI, is shown by Langmuir probe data from a conventional ELMing counter-NBI discharge, also shown in Fig. 6(b), indicating normal minimal E_r values in the SOL.

Counter-NBI is associated with a larger prompt ion loss, and larger fraction of confined ion orbits which cross the separatrix than co-NBI discharges. This can be seen

as follows: with respect to the location of ionization, counter-NBI ion orbits move outwards, while with co-NBI they move inwards. Ions crossing the separatrix should make the electric field inside the separatrix more negative and the field outside more positive, as observed. In addition, the opposite toroidal plasma rotation direction with counter-NBI, as compared with co-NBI, should also result in a more negative E_r well inside the separatrix, such that both rotation and pressure gradient effects produce negative contributions to E_r. Negative shear in E_r, which occurs inside the separatrix, is such as to cause main ion orbit squeezing, while positive shear in E_r, which occurs in parts of the SOL in QH–mode, is such as to cause orbit expansion [17]. Thus, operation with counter-NBI should lead to a deeper, more negative E_r well inside the separatrix and a more positive SOL E_r, which should lead in turn to orbit expansion in the SOL. However, as already mentioned, the Langmuir probe data shown in Fig. 6(b) indicate that the increased E_r in the SOL is associated with QH–mode operation, and not counter-NBI per se.

The hypothesis that ions near the outer plasma midplane are playing a role in the creation of the large radial fields observed in QH–mode is supported by Langmuir probe measurements on the plasma bottom (away from the X–point in an upper single-null plasma), showing a much smaller E_r in the SOL. In addition, the data presented earlier in Fig. 3(d) show that T_i is ~1 keV in the SOL, again consistent with enhanced ion effects in that region.

3.3. The edge harmonic oscillation and enhanced particle transport

In most cases, QH–mode plasmas are associated with the presence of an Edge Harmonic Oscillation (EHO). The EHO is continuous during QH–mode operation and is visible on magnetic, density and temperature fluctuation measurements. As its name implies, the EHO typically has multiple harmonics, with toroidal mode numbers ranging from 1 to 10. The harmonic content can vary both from shot to shot and over time within a single discharge. An example of the frequency spectrum of an EHO as measured by a magnetic probe is shown in Fig. 7. In this particular example n=1–4

components are evident at first, changing to a single, stronger n=3 component later in time. As yet, the specific instability mechanism responsible for the EHO has not been identified. A summary of the characteristics of the EHO and a comparison to the quasi-coherent mode responsible for the ELM-free EDA H–mode regime on C-MOD [18] is shown in Table 1. From these characteristics it is evident that while both the EHO and the quasi-coherent mode result in ELM-free H–mode operation, they are different modes. On DIII–D we have also observed a single example of QDB/QH–mode operation without the EHO, but with a continuous global m=1, n=1 mode which extends to the edge. That controlled density, ELM-free H–mode operation can be obtained via a variety of benign MHD activity on a number of machines is encouraging for the robustness and general applicability of these regimes.

In conventional ELM-free H–modes, the density, impurity content and radiated power all rise monotonically due to the improved particle confinement associated with the edge H–mode transport barrier [19]. In QH–mode plasmas, enhanced particle transport generated by the EHO appears to be responsible for the ability to maintain density and radiated power control in the ELM-free QH–mode regime. Langmuir probe measurements of the ion flux to the divertor strike points show that the flux is almost entirely carried by the EHO harmonics, i.e. the EHO harmonics account for almost 100% of the ion flux to the probe. In addition, the edge density profile at the outer midplane is directly modulated at the fundamental EHO frequency, as shown in Fig. 8. These high spatial (sub-cm) and temporal (25 μs) resolution measurements were made by an FM profile reflectometer system [20]. Other evidence for increased particle transport associated with the EHO includes an increase in D_α emission in the entire divertor chamber and a decrease in line density coincident with EHO onset [6].

An important question with regard to the EHO is its location. Independent, high resolution measurements with both beam emission spectroscopy (BES) [21] and reflectometer systems [20] indicate that the EHO is located at the base of the edge pedestals, at or slightly outside the separatrix. There is excellent agreement between the data from the two systems, Fig. 9, showing that the peak of the density modulation

associated with the EHO is centered ~1 cm outside the separatrix. The BES data also show that the EHO has a large spatial phase shift in the same region.

The modulation of the density profile shown in Fig. 8 might suggest that the above data could be explained by a different model, one in which the EHO actually resides in the plasma core or in the high gradient pedestal region, generating a movement of the entire edge profile. In this case the BES and reflectometer systems would show a peak density oscillation in the pedestal region (due to the steep density gradients), even though the origin of the EHO was actually further in. Such a model would also be in agreement with conventional MHD mode analysis, which would suggest that the EHO is located in the vicinity of the q=3 or 4 surfaces. At present we discount this alternative interpretation on the following grounds: as shown by the inset in Fig. 9(a), the region where the BES and reflectometer systems indicate the EHO peaks is at the base of the edge density pedestal, several cm outside the location of the peak gradients, which occur between densities of $0.7–1.5\times10^{19}$ m^{-3}. If the diagnostics were simply responding to a rigid-body motion of the entire profile then the peak response would be observed further in, in the region of the steepest gradients, which it is not. Other considerations supporting the picture in which the EHO is located at or outside the separatrix were presented in Ref. [6], in particular the lack of any mode signatures located in the vicinity of the q=3 or 4 surfaces.

That the EHO does not originate in the high gradient edge pedestal region is also supported by the following consideration. The EHO is known to cause enhanced particle transport, yet the edge pedestal gradients are as steep as in conventional ELMing H–modes, indicating that there is still a particle transport barrier. Consequently, if the EHO were located in the pedestal this would lead to a contradiction. This contradiction is avoided if the EHO resides at the base of the edge pedestal, such that the region of enhanced particle transport is outside the transport barrier.

The EHO has been observed in some low power co-NBI discharges, but has not resulted in ELM-free operation. Achieving ELM-free operation with an EHO in

balanced or co-NBI discharges would significantly extend the operational utility of the QH–mode regime. A goal of the DIII–D program is to achieve a sufficient understanding of the physics of the EHO and QH–mode operation so as to optimize conditions for achieving QH–mode with co-NBI.

3.4. ELM stabilization

A fundamental question regarding QH–mode operation is what is the mechanism that leads to ELM stabilization? We do not have a definitive answer to this question, but can comment on potential mechanisms. One general stabilization mechanism would be a change in the stability boundary. Specific reasons why the stability boundary might change include ion finite Larmor radius (FLR) stabilization effects [16], a change in the edge current density, or E×B shear effects. With regard to FLR stabilization, it should be noted that the pedestal ion temperatures of 4–7 keV result in larger than usual ion Larmor radii of ≤ 1.5 cm, comparable to the width of the edge pedestal. Additional E×B shear effects in the QH–mode edge are also likely. As shown and discussed above in Section 3.2, the edge E_r well and E×B shear are much larger in the QH–mode edge as compared with conventional co-NBI H–modes.

A potential second general reason for ELM stabilization is that the continuous edge MHD may limit the edge pressure gradient, such that the gradient remains below the stability threshold. To first order, this explanation is inconsistent with the observation that the edge ∇P_e remains the same from the ELMing to the QH–mode phases of individual discharges (Section 3.2 above). In addition, the EHO is believed to be located at the foot of the edge transport barrier, as discussed in Section 3.3 above.

4. CORE ASPECTS OF QUIESCENT DOUBLE BARRIER OPERATION

In this section we consider core related aspects of QDB operation, including high performance operation, transport and fluctuations, and impurity issues.

4.1. High performance

High performance QDB plasmas are created by the addition of core ITBs inside the QH–mode edge. ITB formation is straightforward using standard techniques [8,15]. Relative performance ($\beta_N H_{89}$) improves with higher input power, while absolute performance (β_T, S_n) improves with increasing I_p and B_T. An example of a high performance QDB discharge is shown in Fig. 10. This discharge achieves a constant $\beta_N H_{89}$ product of 7 for 1.6 s (10 τ_E), at I_p = –1.6 MA, B_T = 2.0 T, and P_{NBI} = 11.8 MW. Other parameters for this discharge include $T_i(0)$ = 17 keV, β_N = 2.7%-m-T/MA, H_{89} = 2.6, β = 3.8%, W = 1.58 MJ, τ_E = 160 ms and DD neutron rate $S_n \leq 5.2\times10^{15}$ s^{-1}. In this plasma q_{min} was ~1; plasmas with the EHO typically maintain $q_{min} > 1$. Thus, long pulse high performance QDB operation has been maintained even with $q_{min} \sim 1$ and without sawteeth. The quoted H_{89} factor and confinement times include a correction for prompt beam ion orbit losses. The discharge was beam fueled and there is excellent density and radiated power control throughout the high performance phase, which has a quiescent edge throughout. The high performance phase in this discharge is limited in duration only by NBI source constraints.

The discharge shown in Fig. 10 is the only identified example to date where QDB/QH–mode operation was obtained without an EHO. Instead, this discharge has a continuous global m=1, n=1 mode, commencing at 1.9 s. The global mode is observed in the edge pedestal by density fluctuation diagnostics, and appears to play the same role as the EHO in other discharges. The beneficial role of this mode is also reminiscent of the benign MHD utilized in other DIII–D controlled density, long pulse, high performance discharges [22]. It is important to note that the same level of performance as that shown in Fig. 10 has been obtained in otherwise identical discharges with the more usual EHO (apart from having higher q_{min}, such that the 1/1 mode is not present).

4.2. Core transport and fluctuations

Shown in Fig. 11 is transport analysis by the TRANSP code [23], for the same discharge presented in Fig. 10, with a comparison to a counter-NBI ITB plasma with an L–mode edge. To better show the regions of reduced transport, diffusivities are also plotted from a comparable counter-NBI ITB discharge with an L–mode edge, and a standard L-mode discharge. The two (core and edge) regions of reduced transport in the QDB plasma are clearly visible, with core ion thermal diffusivities reduced to neoclassical levels. As discussed in detail in Ref. [5], a region of reduced E_r shear between the edge and core barriers is believed to be responsible for maintaining the separation between the barriers.

Steady-state modeling using the GLF23 gyro-Landau-fluid transport code [24], replicates the core ion transport barrier in these QDB discharges, Fig. 12(a), though the core electron temperature profile is not accurately predicted. In addition, the GLF23 model shows that the turbulence growth rate and E×B shearing rate γ_E are in approximate balance from $\rho \sim 0.3$ to 0.7, Fig. 12(b), such that complete turbulence stabilization is not expected in this region, in agreement with separate analysis by the linear gyrokinetic stability (GKS) code [25]. These predictions are in agreement with experimental observations; measurements of low-k turbulence by both FIR scattering and reflectometer systems indicate that core turbulence is not eliminated in these plasmas. In the GLF23 model, the formation of the ion transport barrier is still a consequence of the large E×B shear levels regulating the turbulent transport.

Reflectometer measurements of the turbulence radial correlation length Δr, shown in Fig. 13, indicate a substantial reduction in Δr over a measurement range of $0.1 \leq \rho \leq 0.4$ in QDB plasmas. The reduction is by comparison with previous L–mode measurements [26], in which Δr was found to scale approximately as 5–10 ρ_s. A reduction in the turbulence correlation length should be indicative of a reduction in the step size of the turbulent transport, and is occurring in the region of measured transport reduction. This experimental observation of reduced turbulent correlation lengths in

QDB plasmas has been replicated by initial non-linear global gyrokinetic modeling of ITG turbulence using the circular-geometry UCAN code [27]. Further modeling is required to verify this result. Thus, initial turbulence modeling of these QDB plasmas shows agreement with experiment with regard to the ion temperature profile and the behavior of the turbulence amplitude and correlation lengths. That little turbulence amplitude reduction is predicted or seen in regions with neoclassical ion transport will be the subject of further study, via both additional measurements and modeling. Potential mechanisms by which finite turbulence levels can coexist with an ITB are discussed in detail in Ref. [28].

4.3. Impurity transport and prospects for steady-state operation

Impurity transport and accumulation is a major issue for long pulse, high confinement regimes [29]. The constant radiated power in QDB discharges, Figs. 1 and 10, indicates that the edge EHO and global 1/1 mode successfully control the low-Z impurity content as well as the electron density, in strong contrast to the situation with conventional ELM-free H–mode operation [19]. However, high-Z impurities, including nickel, can accumulate during QDB operation, as shown in Fig. 14. Nickel radiation from the plasma center continues to increase slowly throughout this QDB discharge, with a time constant ≥ 500 ms. However, the central carbon content remains constant, i.e. low-Z impurities (carbon) are not accumulating, but high-Z are. These results are replicated by neoclassical impurity transport modeling, using the STRAHL code [30,31]. STRAHL predicts both central accumulation of high-Z impurities due to the high density peaking in these plasmas ($n_e(0)/\overline{n}_e$~2–3), in accord with previous results in other confinement regimes [29], and no preferential carbon accumulation. Spectroscopic analysis and MIST [32] modeling also indicate that for discharge 103818 the nickel had a substantial impact on the total Z_{eff}; without high-Z impurities the total Z_{eff} would have been ~2.4, as opposed to the to the actual total Z_{eff} of ~4.1. In addition, TRANSP [23] analysis indicates that the neutron rate is reduced by ~40–70% compared with what would be obtained if the nickel were absent. This implies that QDB fusion

performance could be substantially improved if the high-Z impurities were reduced. That the measured total radiated power remains constant while the nickel accumulates is explained by the fact that the total power radiated by the nickel is small, < 300 kW.

Experiments have been performed to directly measure high-Z impurity transport rates in QDB discharges in order to determine if the nickel accumulation is due to source or transport effects, and results will be available later in the year. There is evidence in QDB discharges of enhanced plasma-wall interactions, which may provide a strong impurity source. If such a source cannot be confirmed or eliminated, then an alternative solution would be to actively reduce the density peaking. The density peaking has been reduced transiently in QDB plasmas using a variety of techniques, including increasing the plasma triangularity [6], edge impurity injection and off-axis pellet injection.

As discussed in Ref. [5], reducing the density peaking would also have the benefit of improving bootstrap current alignment; QDB plasmas have a bootstrap fraction of up to 45%, but peaked on-axis. In addition, NBCD from counter-NBI generates 10–15% of the total current, but in the opposite direction. Modeling work has been initiated to explore the fully non-inductive, steady-state potential of the QDB regime. Initial conclusions are that the lower densities and higher electron temperatures in QDB plasmas are highly favorable for off-axis ECCD. As might be expected, however, additional on-axis current drive is required to control q_0 in the presence of the significant counter-NBCD. Simulations over 10 s with no ohmic current and using 3 MW of FW for on-axis current drive and 6 MW of off-axis ECCD indicate potential for control of the q profile.

5. CONCLUSIONS

The results reported here demonstrate that sustained, high performance ELM-free H–mode plasmas are possible with good density and radiated power control. The results also demonstrate that the quiescent, ELM-free edge can easily be combined with core ITBs so as to obtain the benefits of both core and edge transport barriers. The

combination of core ITBs and edge H–mode temperature pedestals in the new QDB regime results in high performance plasmas; a $\beta_N H_{89}$ product of 7 has been maintained for 10 τ_E. The double barriers have been maintained for > 3.5 s (~25 τ_E), demonstrating a long-pulse, quasi-steady-state capability. Substantial progress has been made in understanding the processes leading to the creation of the quiescent H–mode edge and characterizing the benign MHD activity associated with QH–mode operation**.** In the plasma core, transport and turbulence measurements are in agreement with initial modeling and simulation results, though more comparisons are required.

ACKNOWLEDGEMENT

This is a report of work supported by the U.S. Department of Energy under Grant Nos. DE-FG03-01ER54615, DE-FG02-89ER53297, DE-FG02-92ER54141, DE-FG03-96ER54373, DE-FG03-95ER54294, DE-FG02-90ER54084, and Contract Nos. DE-AC03-99ER54463, DE-AC05-00OR22725, W-7405-ENG-48, DE-AC02-76CH03073, and DE-AC04-94AL85000.

REFERENCES

[1] ITER Physics Basis Document, Nucl. Fusion **39**, 2137 (1999).

[2] Leonard, A.W., *et al.*, J. Nucl. Mater. **266-269**, 109 (1999).

[3] Lao, L.L., *et al.*, Plasma Phys. Control. Fusion **42**, A51 (2000).

[4] Doyle, E.J., *et al.*, "Progress Towards Increased Understanding and Control of Internal Transport Barriers on DIII–D," Proc. of 18th IAEA Fusion Energy Conf., Sorrento, Italy, 2000 (International Atomic Energy Agency, Vienna), to be published in Nucl. Fusion.

[5] Greenfield, C.M., *et al.*, Phys. Rev. Lett. **86**, 4544 (2001).

[6] Burrell, K.H., *et al.*, Phys. Plasmas **8**, 2153 (2001).

[7] Yushmanov, P.N., *et al.*, Nucl. Fusion **30**, 1999 (1990).

[8] Greenfield, C.M., *et al.*, Phys. Plasmas **7**, 1959 (2000).

[9] Rice, B.W., *et al.*, Nucl. Fusion **39**, 1855 (1999).

[10] Strait, E.J., *et al.*, Phys. Plasmas **4**, 1783 (1997).

[11] Fujita, T., *et al.*, Nucl. Fusion **39**, 1627 (1999).

[12] Kamada, Y., *et al.*, Nucl. Fusion **39**, 1845 (1999).

[13] Söldner, F.X., *et al.*, Nucl. Fusion **39**, 407 (1999).

[14] Wolf, R.C., *et al.*, Plasma Phys. Control. Fusion **41**, B93 (1999).

[15] Rice, B.W., *et al.*, Nucl. Fusion **36**, 1271 (1996), and Phys. Plasmas **3**, 1983 (1996).

[16] Ferron, J.R., *et al.*, Phys. Plasmas **7**, 1976 (2000).

[17] Hinton, F.L., and Kim, Y.-B., Phys. Plasmas **2**, 159 (1995).

[18] Hubbard, A., *et al.*, Phys. Plasmas **8**, 2033 (2001).

[19] Jackson, G.J., *et al.*, Phys. Fluids **B4**, 2181 (1992).

[20] Zeng, L., *et al.*, Rev. Sci. Instrum **72**, 320 (2001).

[21] McKee, G.R., *et al.*, Rev. Sci. Instrum **70**, 913 (1999).

[22] Wade, M.R., *et al.*, Phys. Plasmas **8**, 2208 (2001).

[23] Hawryluk, R.J., in *Proc. of the Course in Physics Close to Thermonuclear Conditions,* Varenna, 1979 (CEC, Brussels, 1980), Vol. I, p.19.

[24] Waltz, R.E., *et al.*, Phys. Plasmas **4**, 2482 (1997).

[25] Waltz, R.E., *et al.*, Phys. Plasmas **6**, 4265 (1999).

[26] Rhodes, T.L., *et al.*, Proc. of the 27th EPS Conf. on Controlled Fusion and Plasma Physics, Budapest, Hungary 2000 (European Physical Society, 2000).

[27] Sydora, R.D., *et al.*, Plasma Phys. Control. Fusion **38**, A281 (1996).

[28] Doyle, E.J., *et al.*, Plasma Phys. Control. Fusion **42**, A237 (2000).

[29] Baker, D.R., *et al.*, Phys. Plasmas **8**, 1565 (2001).

[30] Behringer, K., "description of the impurity transport coide STRAHL," JET-R(87)08, JET Joint Undertaking, Culham, UK (1987).

[31] Peeters, A.G., Phys. Plasmas **7**, 268 (2000).

[32] Hulse, R.A., Nuclear Technologies/Fusion **3**, 259 (1983).

FIGURE CAPTIONS

FIG. 1. Example of the time history of a QDB plasma, 106919, showing: (a) plasma current, (b) central and line average n_e, (c) divertor D_α emission, (d) P_{NBI} and total radiated power, (e) $\beta_N H_{89}$ (the H-factor is corrected for prompt ion orbit losses), and (f) amplitude of magnetic probe signal. The period of quiescent QDB/QH–mode operation is indicated in (c).

FIG. 2. Profiles of (a) T_i, (b) T_e, (c) q and (d) n_e, for three discharges. One is the QDB discharge illustrated in Fig. 1 (106919, red curves), the second is a counter injection ITB discharge with an L–mode edge (99849, blue), and the third is an L–mode discharge (99852, green). The double transport barrier in the QDB plasma is immediately apparent in the temperature profiles (shaded regions), with $T_i(0)$ reaching 16 keV. From (c) it can be seen that the foot of the core transport barriers lies substantially outside $\rho_{q_{min}}$, while the typical low QDB edge densities can be seen in (d).

FIG. 3. Profiles of (a) n_e, (b) T_e, (c) P_e and, (d) T_i in the edge pedestal region of discharge 106919, from both the ELMing and QH–mode phases. The edge gradients are the same or higher in the QH–mode phase as compared with the ELMing phase.

FIG. 4. Comparison of edge pedestal conditions in QH–mode and ELMing regimes. (a) The temperature at the top of the pedestal, T_{e_PED} versus n_{e_PED}, both quantities being determined from Thomson scattering data. Both axes are normalized by the Greenwald density, n_{GW}. (b) Maximum edge pressure gradient $2\alpha_e$, normalized to the ideal ballooning mode critical gradient, versus the triangularity δ away from the X–point. α is the normalized pressure gradient (ballooning parameter), $\alpha = -q^2 R_o \nabla\beta$, where R_0 is the mean major radius.

FIG. 5. Comparison of the heat flux to the outer divertor strike point for three discharges, a high density ELMing H–mode ($\bar{n}_e$ = 8×10^{19} m^{-3}, P_{NBI} = 4.5 MW,

101560), a low density ELMing H–mode ($\bar{n}_e$ = 3.6×10^{19} m^{-3}, P_{NBI} = 6.25 MW, 104274) and a QDB discharge ($\bar{n}_e$ = 2×10^{19} m^{-3}, P_{NBI} = 7 MW, 105836).

FIG. 6. (a) Comparison of the edge radial electric field E_r, as determined from charge exchange recombination (CER) measurements, in a QH–mode discharge (103818) and a conventional ELM-free co-NBI discharge (100164), at comparable input power. (b) Comparison of the SOL E_r, as determined from Langmuir probe measurements, in a QH–mode discharge (106996) and in an ELMing counter-NBI discharge (103721).

FIG. 7. Contour plot of the frequency spectrum of a magnetic probe signal from a QDB discharge (106996) as a function of time. The spectrum shows multiple EHO harmonics with toroidal mode numbers n=1–4, and time varying harmonic content.

FIG. 8. For discharge 106939, (a) time history of the signal from a 15 GHz fixed frequency reflectometer, illustrating the EHO oscillation at a density layer of 2.8×10^{18} m^{-3}. (b) Contour plot of the spatial location of SOL density layers as a function of time, as measured by a profile reflectometer system. By a comparison of (a) and (b) it is apparent that the EHO is modulating the position of the SOL density layers.

FIG. 9. Reflectometer [(a) and (b)] and BES [(c) and (d)] data relating to the location of the EHO for discharge 106926. (a) Radial profile of the density fluctuations associated with the EHO, as determined from the reflectometer data, showing a peak ~1 cm outside the separatrix. (b) Edge density profile as measured by a profile reflectometer system, with an inset showing the location of the main plot with respect to the edge pedestal. (c) Radial profile of the density fluctuations associated with the n=2 component of the EHO, as determined from the BES system, again showing a peak ~1 cm outside the separatrix and, (d) radial phase shift of the EHO n=2 component.

FIG. 10. Example of the time history of a high performance QDB plasma (106956), showing: (a) plasma current, (b) central and line average n_e, (c) divertor D_α emission, (d) P_{NBI} and total radiated power, (e) $\beta_N H_{89}$ (the H-factor is corrected for prompt ion

orbit losses) and, (f) neutron rate. The period of quiescent QDB/QH–mode operation is marked in (c). This discharge achieves $\beta_N H_{89}$=7 for $10\tau_E$.

FIG. 11. Profiles of (a) χ_i and χ_i neoclassical (dashed lines) and, (b) χ_e, for three discharges. One is the QDB discharge illustrated in Fig. 10 (106956, red curves), the second is a counter injection ITB discharge with an L–mode edge (99849, blue), and the third is an L–mode discharge (99852, green). Ion thermal diffusivities are reduced to neoclassical levels in the core of the ITB discharges.

FIG. 12. GLF23 modeling of QDB discharge 103740. Shown in (a) is the GLF23 steady-state prediction for the ion and electron temperature profiles, with a comparison to the actual experimental profiles, while (b) shows a comparison of the maximum calculated turbulence growth rate γ_{MAX} to the E×B shearing rate γ_E.

FIG. 13. Reflectometer measurements of the turbulence radial correlation length Δr, compared with 5–10 ρ_s, for (a) an L–mode data set, and (b) a QDB data set. The correlation lengths are much smaller in the core of QDB plasmas as compared with the scaling observed in L–mode, indicating a reduced step size for turbulent transport.

FIG. 14. Time histories of impurity related quantities for QDB discharge 106940, showing (a) P_{NBI} and total radiated power, (b) divertor D_α emission, (c) central and line average n_e, (d) Ni XXV and XXVI line emission intensities and, (e) central carbon fraction. The central nickel content (Ni XXVI) accumulates with a time constant ≥ 500 ms.

Table 1.—Characteristics of edge oscillations in the ELM-free Quiescent H–mode on DIII–D and EDA H–mode on C-MOD

	Edge Harmonic Oscillation (DIII–D)	Quasi-Coherent Mode (C–Mod)
Increases D_α level in divertor	Yes	Yes
Increases particle transport across separatrix	Yes	Yes
Location	Foot of edge barrier	Edge density barrier
Frequency	6–10 kHz (n=1)	60–200 kHz
Toroidal mode number	Multiple, variable mix n=1–10	Unknown
Poloidal wavelength	~100 cm (m ~ 5)	~1 cm
Edge collisionality	Collisionless	Collisional

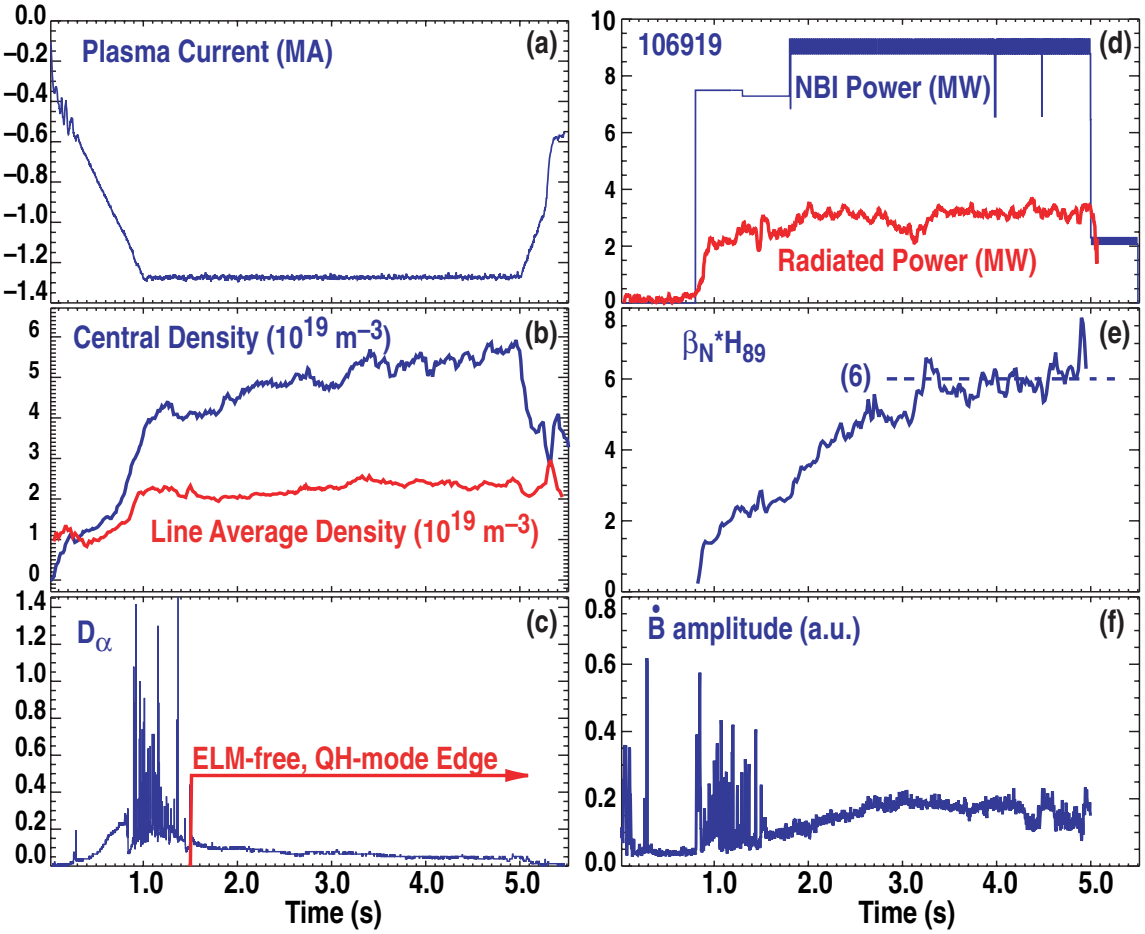
Plasma Current (MA)
(a)
Central Density (10^{19} m^{-3})
Line Average Density (10^{19} m^{-3})
(b)
D_α
ELM-free, QH-mode Edge
(c)
106919
NBI Power (MW)
Radiated Power (MW)
(d)
β_N*H_{89}
(6)
(e)
$\dot{B}$ amplitude (a.u.)
(f)
Time (s)
Time (s)

Figure 1.

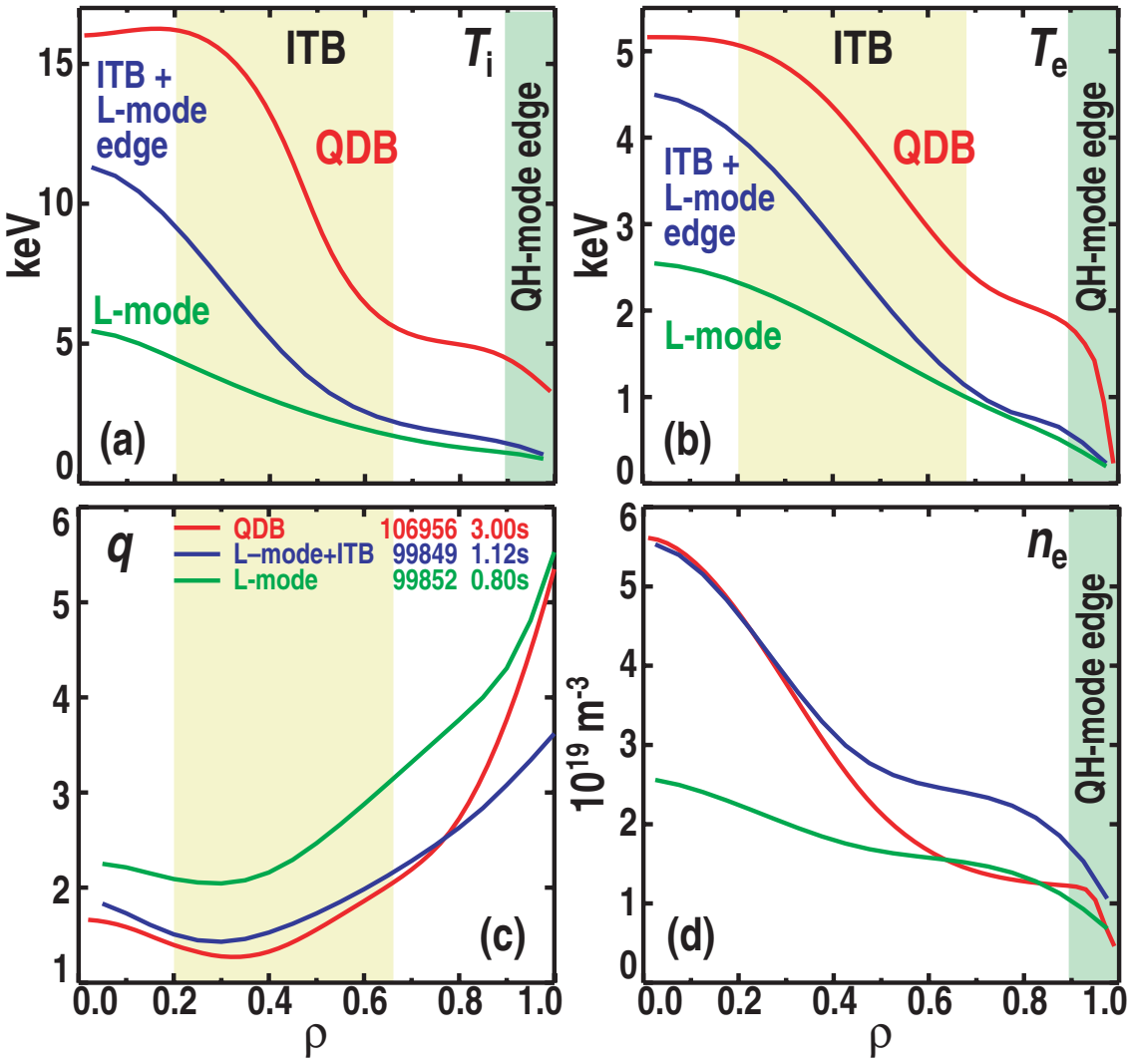
ITB
T_i
ITB +
L-mode
edge
QDB
L-mode
QH-mode edge
keV
(a)
ITB
T_e
QDB
ITB +
L-mode
edge
L-mode
QH-mode edge
keV
(b)
q
QDB 106956 3.00s
L–mode+ITB 99849 1.12s
L-mode 99852 0.80s
(c)
ρ
n_e
QH-mode edge
10^{19} m^{-3}
(d)
ρ

Figure 2.

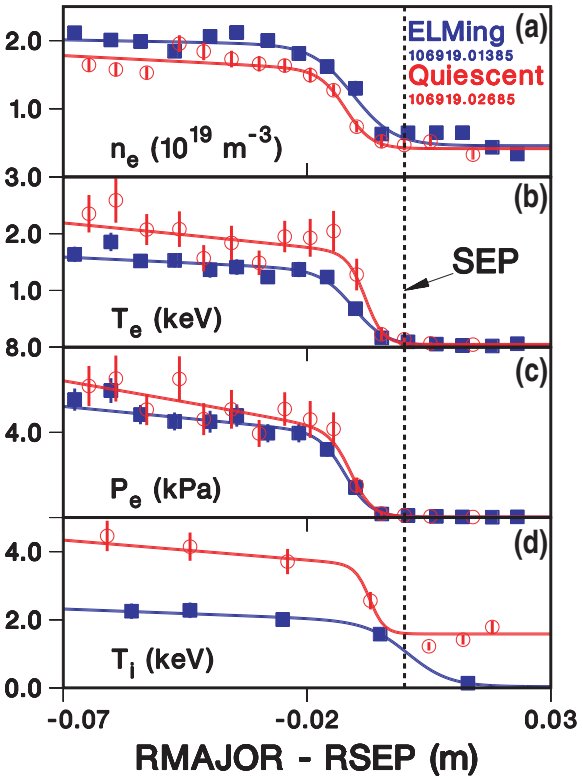

Figure 3.

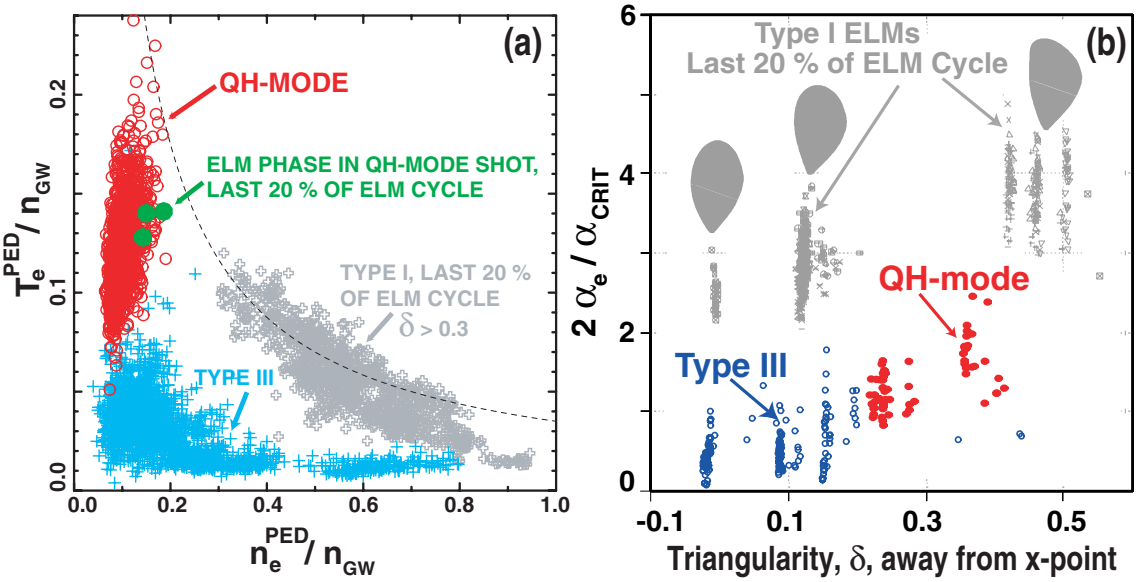

Figure 4.

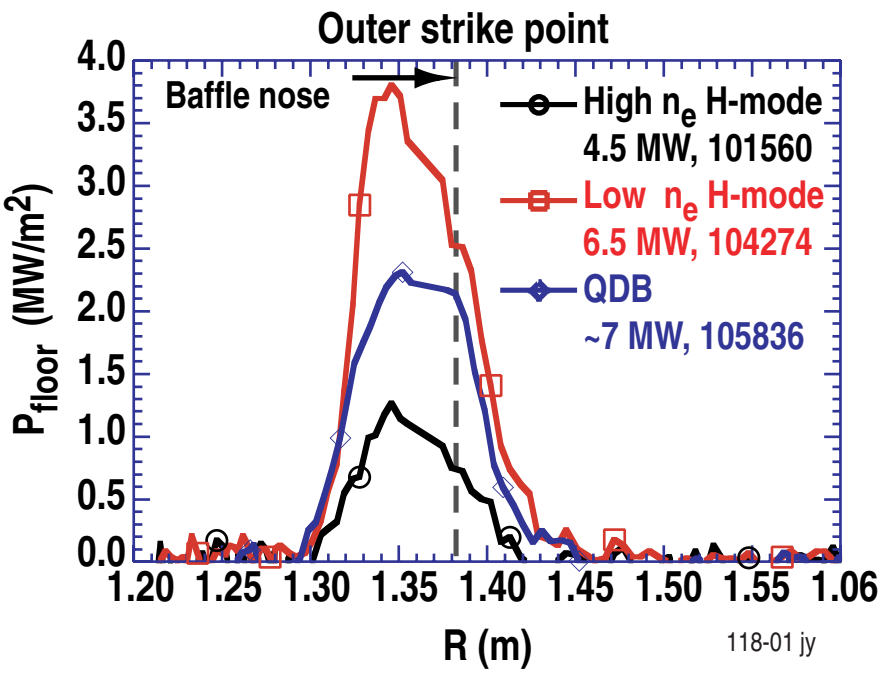

Figure 5.

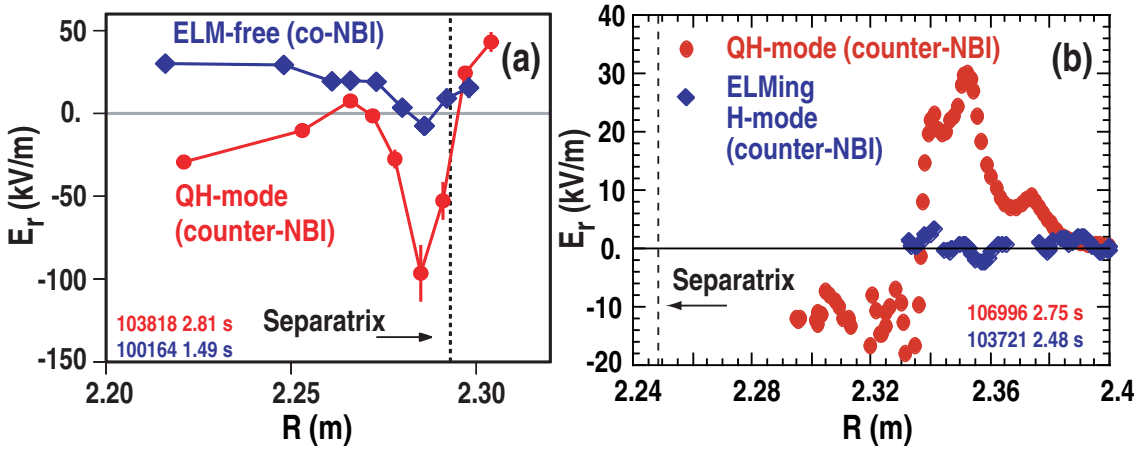

Figure 6.

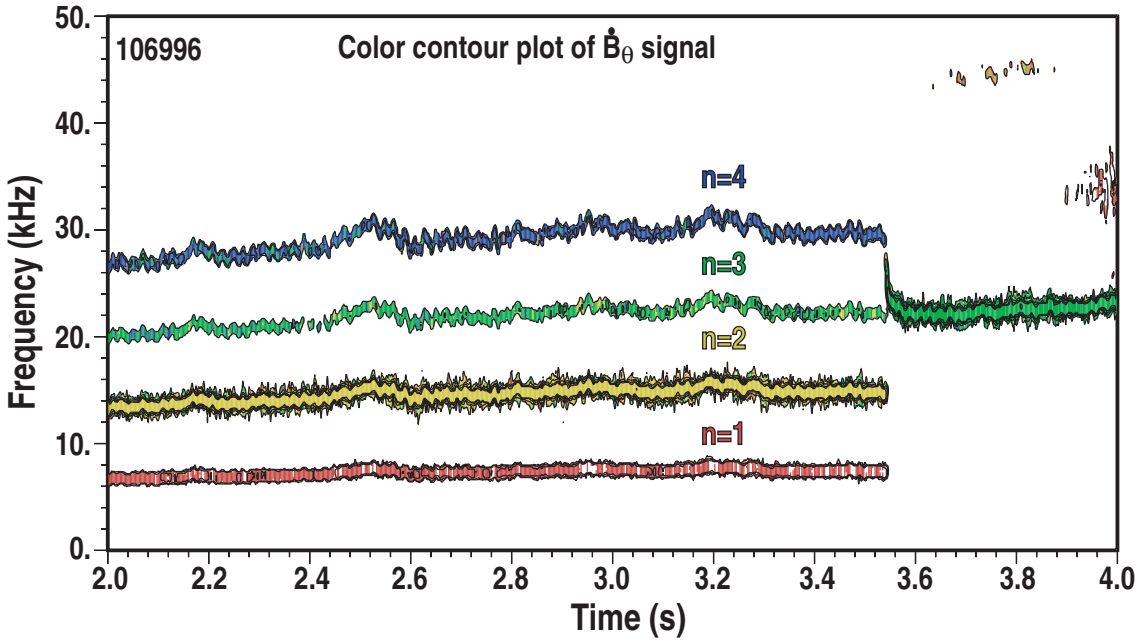
106996
Color contour plot of $\dot{B}_\theta$ signal
Frequency (kHz)
Time (s)
n=4
n=3
n=2
n=1
50.
40.
30.
20.
10.
0.
2.0
2.2
2.4
2.6
2.8
3.0
3.2
3.4
3.6
3.8
4.0

Figure 7.

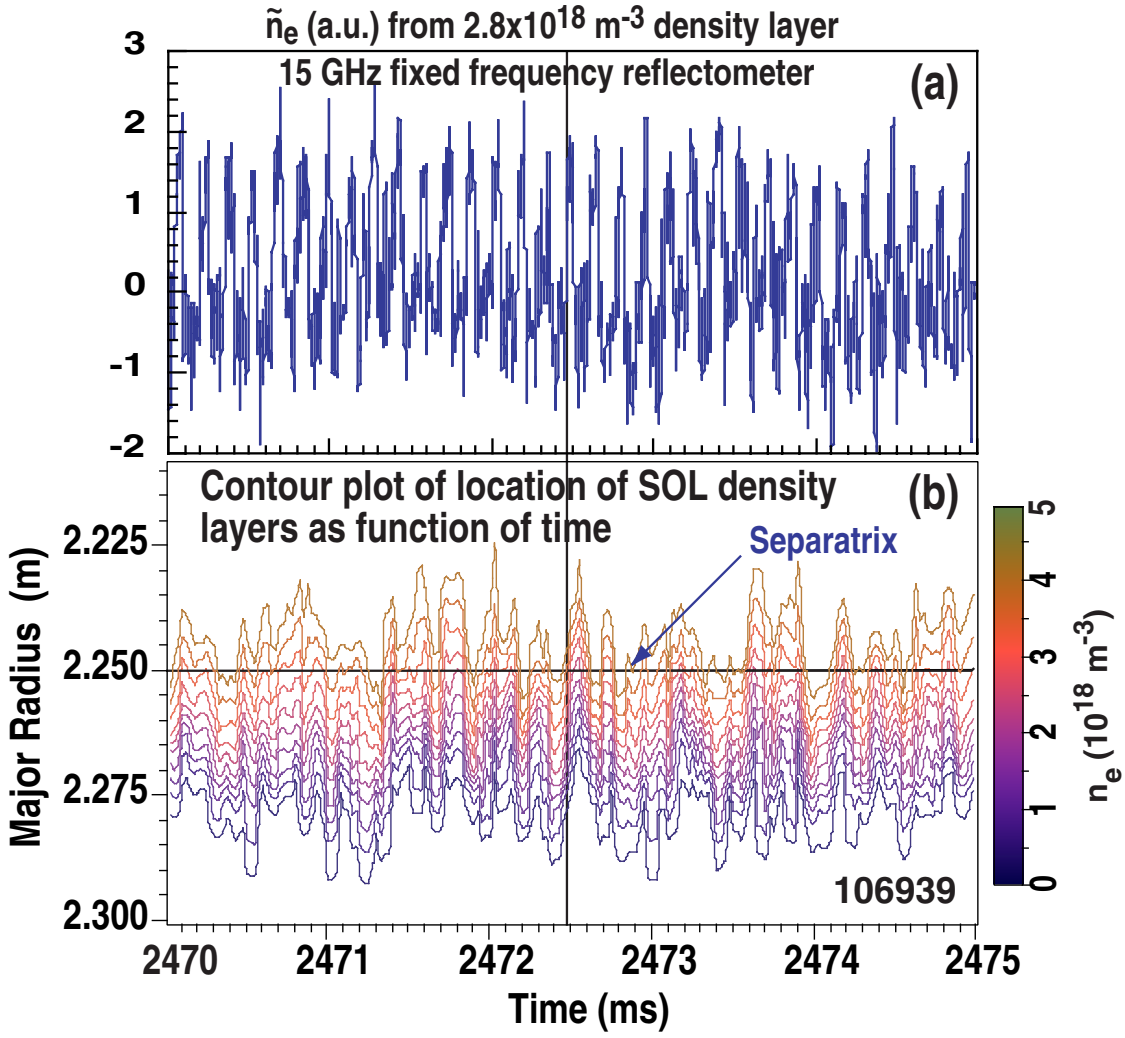
$\tilde{n}_e$ (a.u.) from 2.8x10^{18} m^{-3} density layer
15 GHz fixed frequency reflectometer
(a)
3
2
1
0
-1
-2
Contour plot of location of SOL density layers as function of time
(b)
Separatrix
106939
Major Radius (m)
2.225
2.250
2.275
2.300
2470
2471
2472
2473
2474
2475
Time (ms)
n_e (10^{18} m^{-3})
0
1
2
3
4
5

Figure 8.

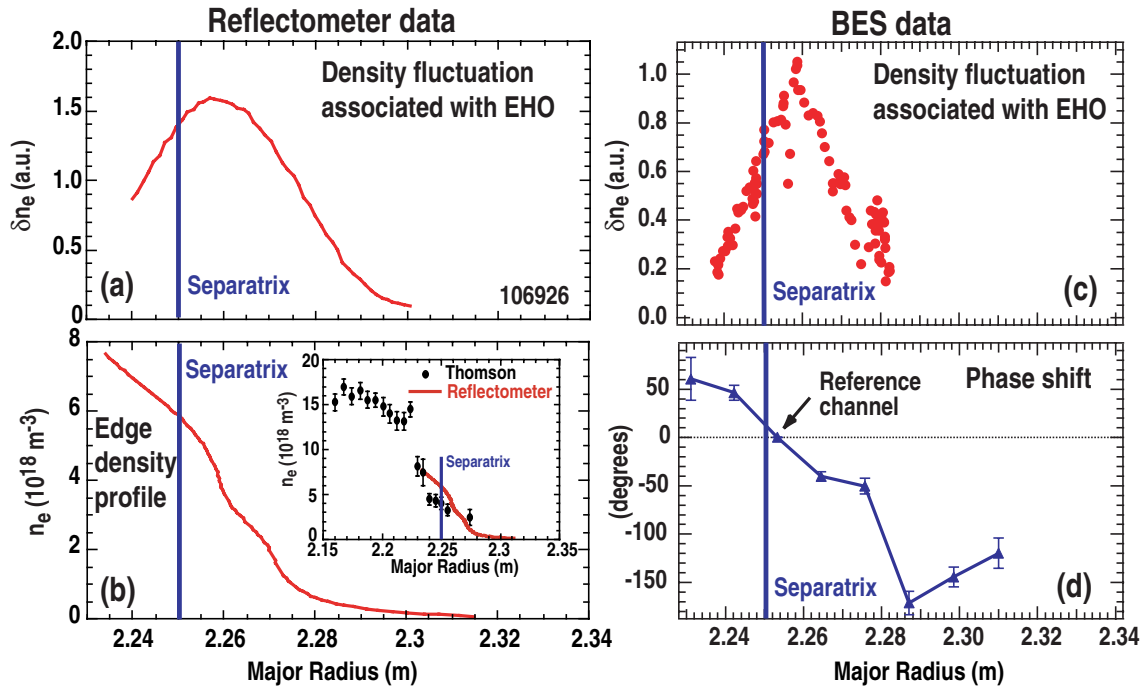
Reflectometer data
BES data
Density fluctuation
associated with EHO
Separatrix
106926
(a)
(b)
(c)
(d)
Edge
density
profile
Thomson
Reflectometer
Reference
channel
Phase shift
δne (a.u.)
ne (10^18 m^-3)
(degrees)
Major Radius (m)

Figure 9.

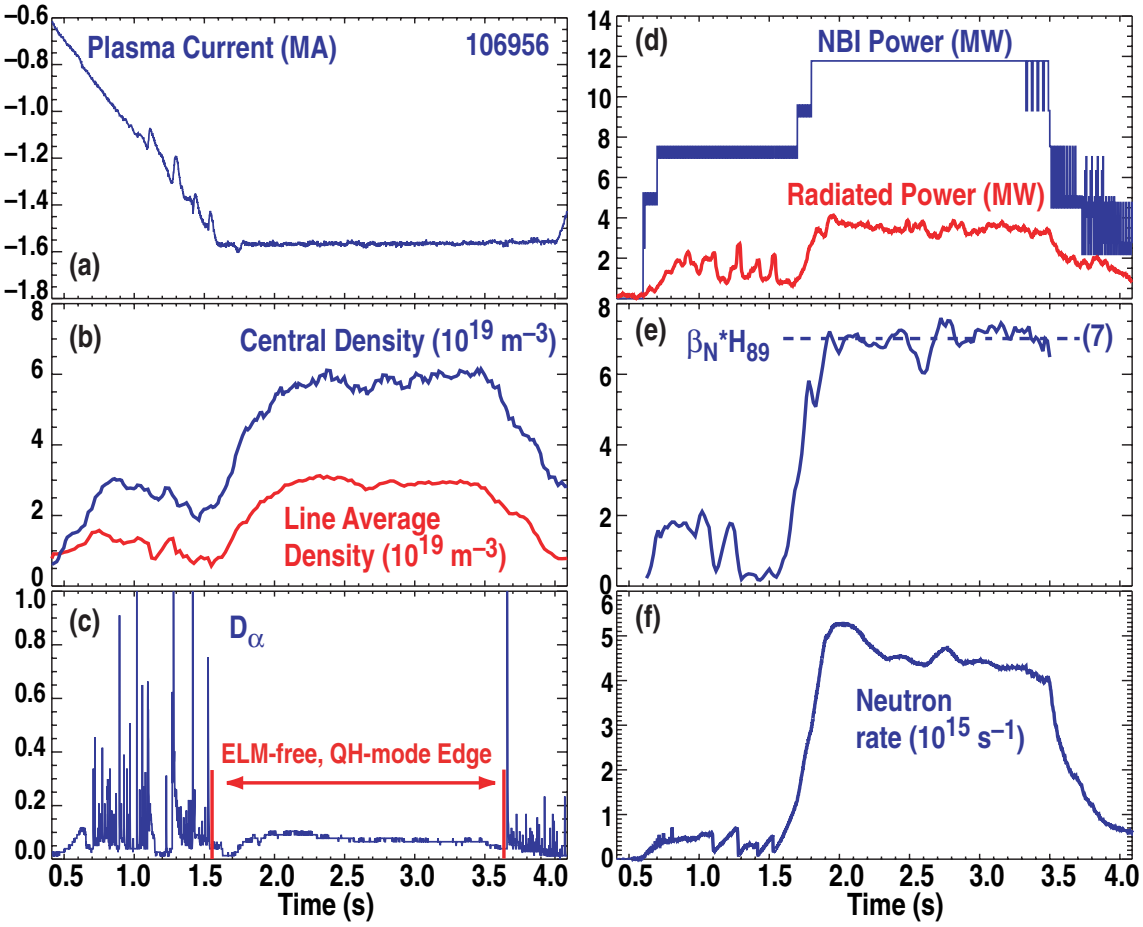
Plasma Current (MA)
106956
(a)
(b)
Central Density (10^{19} m^{-3})
Line Average
Density (10^{19} m^{-3})
(c)
D_α
ELM-free, QH-mode Edge
Time (s)
(d)
NBI Power (MW)
Radiated Power (MW)
(e)
β_N*H_{89} - - - - - - - - (7)
(f)
Neutron
rate (10^{15} s^{-1})
Time (s)

Figure 10.

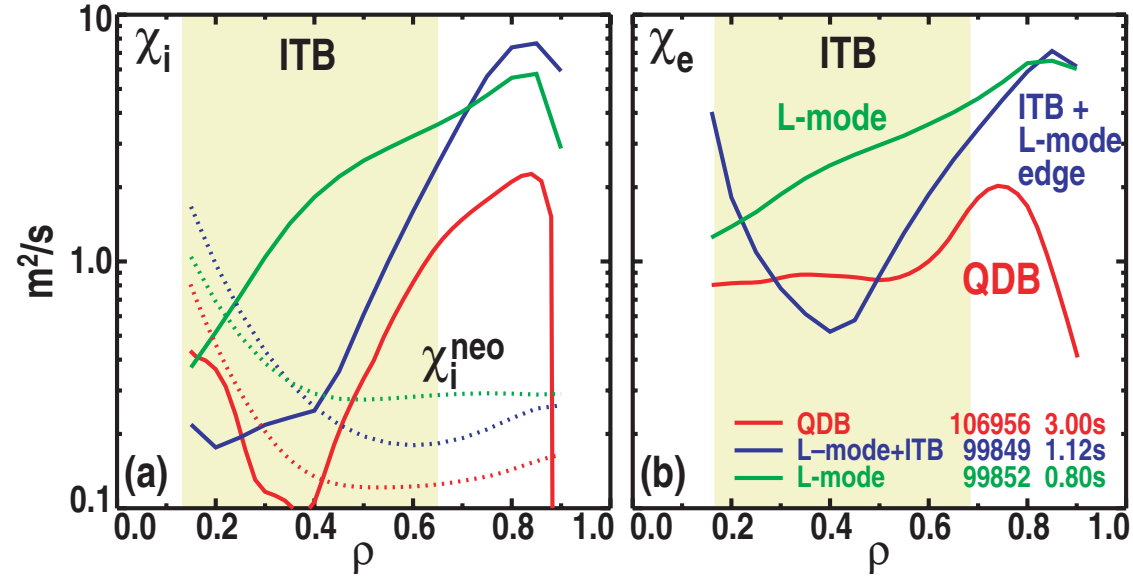

Figure 11

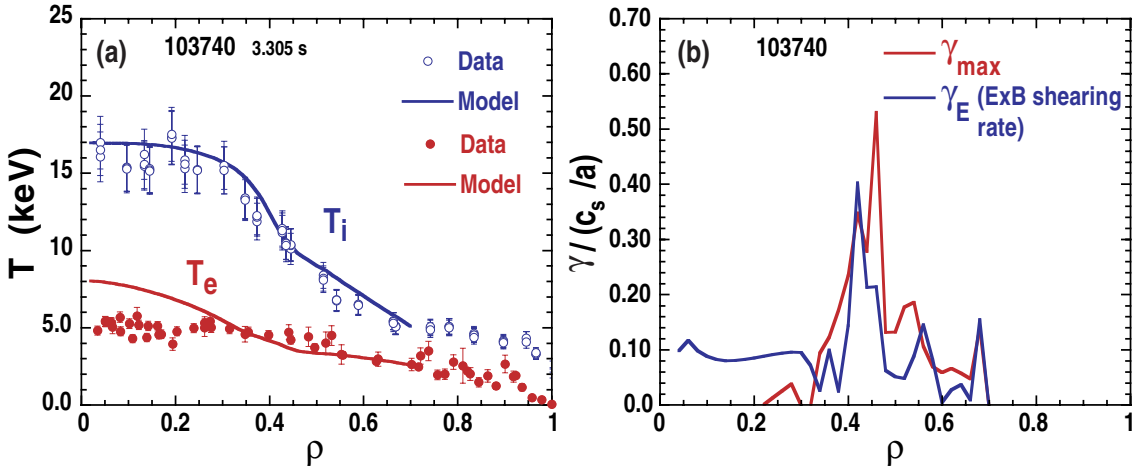

Figure 12.

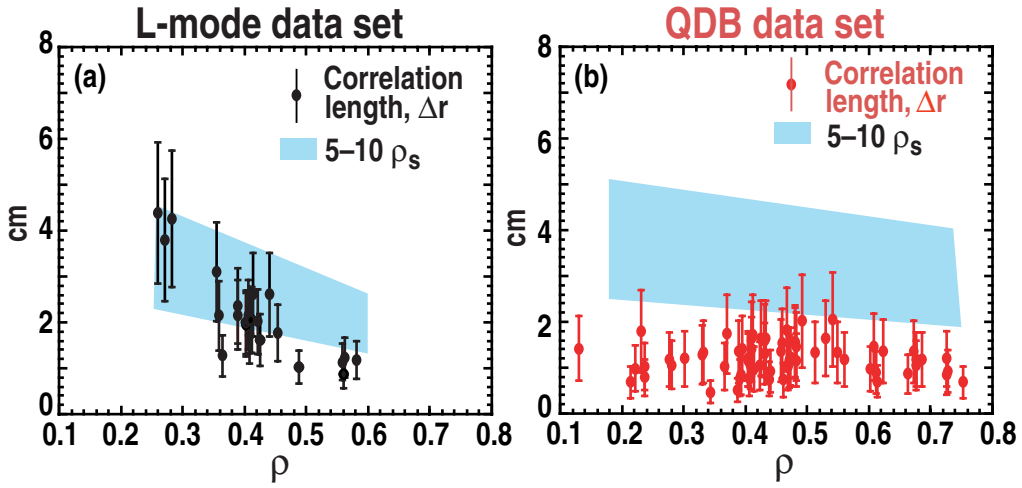

Figure 13.

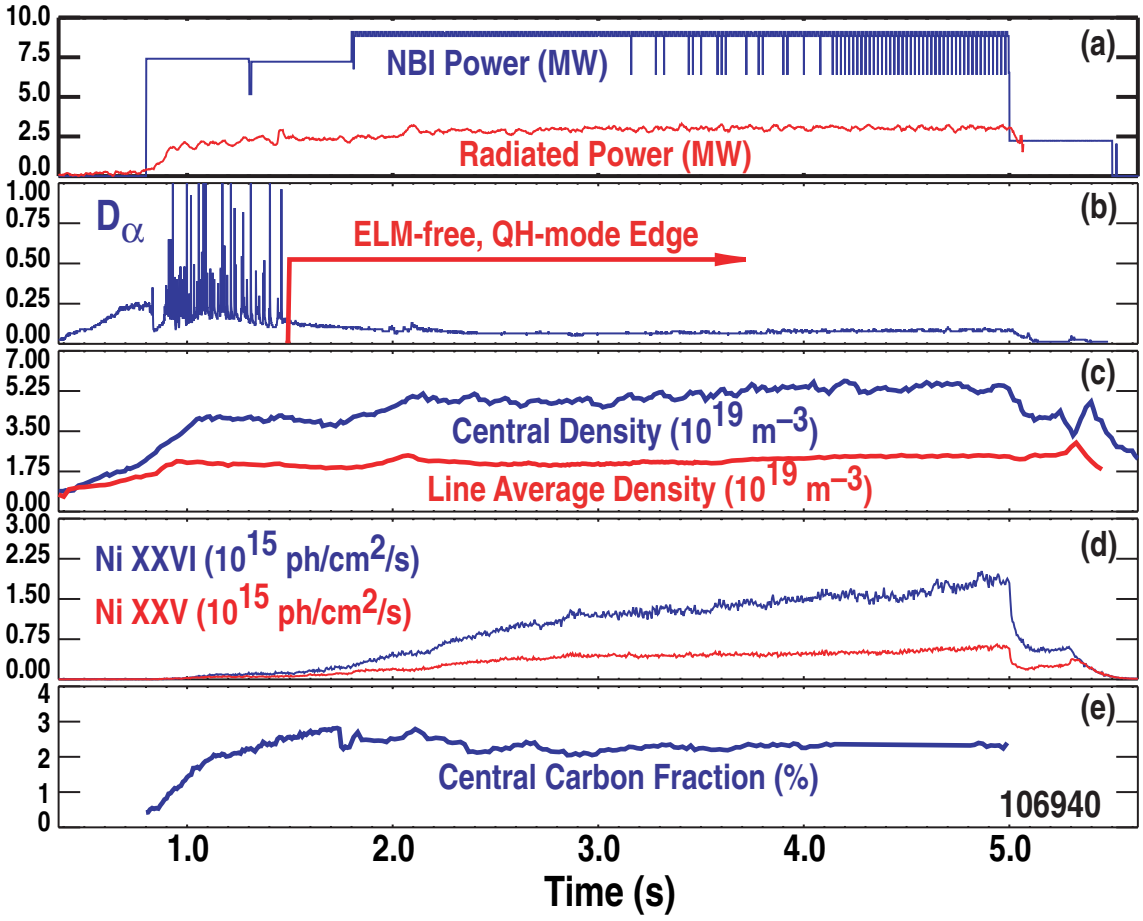

Figure 14.